THE JOURNAL OF PHYSICAL CHEMISTRY C

Article

Cite This: J. Phys. Chem. C 2019, 123, 11020−11031

pubs.acs.org/JPCC

Influence of Crystal Facet and Phase of Titanium Dioxide on Ostwald Ripening of Supported Pt Nanoparticles from First-Principles Kinetics

Qixin Wan,[†,§,⊥] Sulei Hu,[‡,∥,⊥] Jiangnan Dai,[†] Changqing Chen,[*,†] and Wei-Xue Li[*,‡,∥]

[†]Wuhan National Laboratory for Optoelectronics, Huazhong University of Science and Technology, Wuhan 430074, China

[‡]Department of Chemical Physics, School of Chemistry and Materials Science, iChEM, CAS Center for Excellence in Nanoscience, University of Science and Technology of China, Hefei 230026, China

[§]Key Laboratory for Optoelectronics and Communication of Jiangxi Province, Jiangxi Science and Technology Normal University, Nanchang 330013, China

[∥]Hefei National Laboratory for Physical Sciences at the Microscale, Hefei 230026, China

Supporting Information

ABSTRACT: Metal oxide plays an important role on stability and catalytic performance of supported metal nanoparticles, but mechanistic understanding of structure sensitivity and optimization of the oxide supports remains elusive in heterogeneous catalysis. Taking Ostwald ripening of platinum nanoparticles supported on titanium dioxide (TiO_2) as an example, we reveal here a great structure sensitivity of oxide facets and crystal phases on sintering of supported metal nanoparticles through first-principles kinetic simulation. Total activation energies of the Pt ripening on various pristine TiO_2 surfaces of both anatase and rutile phases are calculated by density functional theory, and Ostwald ripening under isothermal condition and temperature programmed condition are simulated numerically. Calculated total activation energies are found inversely proportional to the corresponding oxide surface energies, and vary considerably from 1.76 to 3.56 eV. The Pt ripening rate on the pristine TiO_2 surfaces follows the order of r(001) ≈ a(001) ≫ a(100) ≈ r(101) > r(100) > a(101) ≈ r(110). For TiO_2 support exposing different facets, not only their intrinsic ripening rate but also their relative surface area determines the overall ripening kinetics and formation of transit bimodal particle size distribution. For pristine anatase TiO_2 exposing a(001) and a(101) facets, ripening starts on a(101) facets only after ripening on a(001) facets finishes due to their order of magnitude difference in ripening rate, resulting a step-wise increase of average particle size with ripening time. For pristine rutile TiO_2 exposing r(101) and r(110) facets, ripening could proceed simultaneously on both facets due to their modest difference in ripening rate, and the average particle size increases monotonically with ripening time. Compared to rutile TiO_2, anatase TiO_2 supports are less resistant to the metal nanoparticles ripening since a(001) facets with high ripening rate is likely to be exposed. The present work is compared to available experiments and the theoretical framework established could be expanded to various metal and oxide systems.

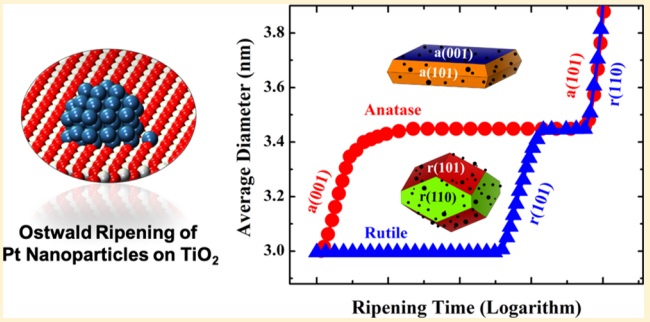

1. INTRODUCTION

Metal nanoparticles (NPs) have received considerable attentions due to the importance in various fields, especially in heterogenous catalysis.[1−3] A large number of low coordination sites exposed increase dramatically the catalytic activity of metal NPs with cost of stability. These NPs are prone to sinter via particle migration and coalescence (PMC) or Ostwald ripening (OR) by lowering the overall surface energies, and accordingly the active surface area and particle-size-specific properties decreases with time.[4−7] The metal−support interaction (MSI),[8] among other, affects critically the corresponding sintering kinetics.[9] It was found that strong metal particle−support interaction could suppress the PMC process by decreasing the diffusion coefficient of supported metal NPs,[10] whereas strong metal atom−support interaction would promote the OR process by lowering the total activation energy of ripening.[11] Mechanistic investigation of these MSIs and their influence on the sintering kinetics are therefore important to improve the overall stability of supported metal NPs.

High surface area of oxide supports are often inhomogeneous, and composed of for instance different crystal faces and numerous defects and imperfections.[12−15] This heterogeneity significantly impacts the MSIs, and accordingly the sintering

Received: February 28, 2019
Revised: March 28, 2019
Published: April 5, 2019

DOI: 10.1021/acs.jpcc.9b01942
J. Phys. Chem. C 2019, 123, 11020−11031

kinetics and the corresponding stability of supported metal NPs.[16−18] Among others, the influence of different oxide surfaces received particular attentions. It was found that metallic Cu NPs were more stabilized and better dispersed on ceria nanospheres exposing mainly (111) surfaces than those on the ceria nanorods and nanocubes exposing mainly (110) and (100) surfaces.[19] During alternating oxidation and reduction, Pt redispersion was found to happen only on ceria nanocubes, rather than on ceria nanooctahedra.[20] In situ sintering investigation of Au NPs on anatase TiO_2 (denoted as a-TiO_2) found that the sintering happens on (101) surfaces (denoted as a(101)), whereas no sintering on a(001) surfaces was observed under the same conditions.[21] For CO oxidation on a-TiO_2 supported Pt NPs, a(100) and a(101) surfaces were found to stabilize highly dispersed and active Pt species and avoid effectively the Pt sintering, compared to a(001) surfaces.[22] Despite extensive study so far, it remains elusive to fully uncover the influence of different oxide surfaces on sintering kinetics.

Oxide supports could in addition exist in different crystal phases, and their different symmetries and surface structures could affect the corresponding catalytic activity and stability of the supported metal NPs as well. For selective hydrogenation of isoprene, Ni NPs supported on γ-Al_2O_3 had a higher stability than that on κ-Al_2O_3.[23] Titanium dioxide, as the supports of interest in the present work, could occur in different crystal phases including rutile, anatase and brookite.[24−26] Their effects on stability of supported NPs have been found in various catalytic reactions.[27−32] For instance, the particle size of Ru on a-TiO_2 support was found to increase with the calcination temperature, whereas these NPs remained stable on the rutile phase of P25 (a mix of anatase and rutile TiO_2 with ratio of 4:1) showing similar sizes at even higher calcination temperatures.[33] Moreover, for supported Ru NPs, pure rutile TiO_2 (r-TiO_2) as supports lead into not only a smaller but also narrower particle size distribution (PSD), compared with pure a-TiO_2 supports.[34] High sintering resistancy of r-TiO_2 supported cobalt particles than that on a-TiO_2 supports was also reported during Fischer−Tropsch synthesis. The stronger MSI of r-TiO_2 with metal NPs than that of a-TiO_2 supports was proposed responsible for the high sintering resistancy observed. On the other hand, different TiO_2 phases have different types of defects, which may be important in the MSIs and the sintering kinetics. Nevertheless, how the crystal phase of oxide affects sintering of supported metal NPs is largely unknown yet at the microscopic point of view.

Previously we established an atomistic theory of OR and disintegration of the supported metal NPs under reaction conditions.[36] Influence of MSI,[11] PSD[37] and reactants[38] on the ripening as well as influence of reactants on disintegration[39] were studied in details. Recently, we reported a first-principles kinetic investigation of ripening of the late transition metals on rutile TiO_2(110) surfaces.[40] To address the role of the oxide facets and crystal phase on sintering of supported transition metal NPs described above, we present here a first-principles based kinetic study of Pt ripening on various crystal surfaces and morphologies of both anatase and rutile TiO_2. For general trend understanding and simplification, we neglected the PMC process, and focused only on the pristine TiO_2 without interfering defects, imperfections and reactants etc. The key parameter, the total activation energies of Pt ripening on various surfaces of anatase and rutile TiO_2 were calculated by density functional theory (DFT). The evolution of PSD[41−43] and average diameter of Pt NPs were explored under both isothermal conditions and temperature programmed conditions. Influence of morphology for both anatase and rutile TiO_2[44−50] were investigated in great details.

2. THEORETICAL METHOD

2.1. Ripening Kinetics. Rate equation of OR for supported NPs was described in details by Parker and Campbell,[51] and generalized rate equation for OR and disintegration applicable under reaction conditions can be found in our earlier work.[36] In brief, for the supported particle with a given curvature radius R, the corresponding rate equation under the steady state is

$$\frac{dR}{dt} = A(R)\exp\left[-\frac{E_{tot}}{k_BT}\right]\left(\exp\left[\frac{\Delta\mu(R^*)}{k_BT}\right] - \exp\left[\frac{\Delta\mu(R)}{k_BT}\right]\right) \quad (1)$$

There are three parts in above equation, namely, the prefactor A(R), total activation energy E_{tot} and chemical potential $\Delta\mu(R)$. Prefactor $A(R) = XY/(X + Y) \times K/R^2$ mainly describes about the ripening mechanism including the interface-limit control and diffusion-limit control, where $X = 2\pi a_0 R \sin(\alpha)$, $Y = 2\pi a_0^2/\ln[L/R \sin(\alpha)]$ and $K = \nu_s\Omega/[4\pi a_0^2\alpha_1]$. α is contact angle between metal NP and support. a_0 is the lattice constant of the support surface, L is the diffusion length of the monomer, ν_s is the vibrational frequency of the monomer on the support surface, Ω is the molar volume of bulk metal atom, $\alpha_1 = (2 - 3\cos\alpha + \cos^3\alpha)/4$ is geometrical factor, k_B is Boltzmann constant, T is temperature.

The total activation energy E_{tot} of ripening is sum of the formation energy of the metal monomer on supports with respect to bulk metal counterpart E_f and the diffusion barrier of the metal monomer on supports E_d. Under the steady state, E_f determines the far-field equilibrium concentration of the monomer on supports, and E_d determines diffusivity of monomer on supports, both depending on MSI. The stronger the MSI, the lower E_f, and the higher the far-field equilibrium concentration of the monomer will be. When potential energy surface for the monomer diffusion on supports is flat, the corresponding diffusion barrier would be lower. All these would increase the ripening rate.

The chemical potential of the atoms for the supported particles with a given R, $\Delta\mu(R)$, indicates the extent of energy raising with respect to the bulk metal counterpart. As a result, corresponding equilibrium concentration of the monomer increases. For particles with different sizes, their equilibrium concentrations are different, and this introduces essentially a driven force for the net flux of the monomers from the smaller particles to the larger ones. In mean field approximation, R^* is the critical radius at which the corresponding particle will neither grow nor shrink. When the particle of interest is larger than R^*, according to eq 1, the derivate of the curvature radius with time has a positive sign, and corresponding particles will grow. In present work, $\Delta\mu$ is approximated by Gibbs−Thomson relation, $\Delta\mu(R) = 2\Omega\gamma/R$.[52] Note that the particle morphology,[53] the particle size,[54] MSI[55−57] and the adsorption of reactants on particles[58] could in addition influence corresponding $\Delta\mu$. More discussion of their influences on the ripening rate can be found in our recent studies.[11,36,38,39]

To simulate the ripening process, the initial average (projection) diameter of NPs $\langle d_0\rangle$ and the relative standard

DOI: 10.1021/acs.jpcc.9b01942
J. Phys. Chem. C 2019, 123, 11020−11031

deviation (rsd) on all the surfaces considered were set as 3 nm and 10% respectively, if not specified otherwise. For temperature programmed aging, the initial temperature of 200 K and heating rate of 1 K/s are used. Our recent work showed that the influence of the contact angle α and surface energy γ of supported NPs on ripening is much less than that of the total activation energy E_{tot}.[11] Accordingly, as a good approximation, α = 90° and γ(Pt) = 155 meV/Å^2[59] as typical values for supported Pt NPs are used though out the present work. Note that for α = 90°, $\langle d \rangle = 2R$.

To study the influence of oxide morphology on ripening of support metal NPs, total activation energies of ripening on individual facets exposed were adopted from the corresponding pristine surfaces calculated by DFT as described below. Moreover, the initial density of the particle number on all facets considered was assumed same, and the monomer diffusion crossing different facets was not considered at the moment. Taking the morphology effect into account, the evolution of the overall particle number was summation of the individual facets weighted by the corresponding surface ratio

$$N = \sum_i f_i N_i \tag{2}$$

where i means the ith facet exposed, f_i is the corresponding percentage exposed. The evolution of PSD, average diameter and normalized dispersion were derived similarly.

2.2. DFT Calculations. To calculate the total activation energy E_{tot} of the Pt ripening on individual oxide surfaces and the corresponding surface energy γ of TiO_2, DFT calculations were performed using the Vienna Ab initio Simulation Program (VASP[60,61]). The projector-augmented wave method together with revised Perdew–Burke–Erzernhof exchange–correlation functional[62] was used, and the kinetic energy cutoff for the plane wave basis set was 400 eV. The spin polarization was not considered in the calculations due to its negligible influence for the Pt/TiO_2 system.[63] The optimized crystal parameters of bulk anatase and rutile TiO_2 are a = 3.826 Å, c = 9.637 Å and a = 4.661 Å, c = 2.968 Å respectively. These results are in good agreement with corresponding experimental values of a = 3.872 Å, c = 9.616 Å[64] and a = 4.593 Å, c = 2.958 Å.[65]

The total activation energy E_{tot} is summation of E_f and E_d, and E_f is calculated via

$$E_f = E_{ma/ox} - E_{ox} - E_B \tag{3}$$

where $E_{ma/ox}$ is the total energy of the Pt monomer on support, E_{ox} is the total energy of the support, and E_B is the total energy of the bulk metal. For adsorption and diffusion of the Pt monomer on TiO_2 surfaces considered, the slab thickness of anatase and rutile TiO_2 were at least 12 Å separated by a 15 Å vacuum layer. Pt atom was adsorbed on one side of the slab, and the top two Ti–O layers and the adsorbates were allowed to relax and the other atoms in the bottom layers were fixed in their bulk-truncated positions. The systems were relaxed by using the conjugate-gradient algorithm until the Hellman–Feynman force[66] on each atom was less than 0.03 eV/Å. Here, (3 × 3), (1 × 3), and (1 × 3) of the surface supercell are considered for anatase (001) (denoted as a(001)), a(100), and a(101) facets respectively, while (3 × 3), (3 × 4), (3 × 3), and (2 × 4) of the surface supercell are considered for rutile (001) (denoted as r(001)), r(100), r(101), and r(110) facets respectively. The Γ point was used to sample the surface Brillouin zone, as done in previous studies.[39,67] It was well documented that generalised gradient approximation functional could not describe properties of TiO_2 and Hubbard U correction could improve the accuracy.[68] To see its influence, E_f was calculated at $U_{eff} = U - J$ = 4.5 eV, and was found to vary in maximum by 0.33 eV on r(110) surface (Figure S1). Compared to the difference of E_f between r(110) and r(001) by 2.74 eV, Hubbard U correction is small and not considered in present work. The climbing image nudged elastic band[69,70] method was used to calculate the diffusion barrier E_d of the Pt monomer on surface. At least 7 images (including the initial and final positions) were used, and the transition states optimized were confirmed by vibrational analysis showing a single imaginary mode. Zero-point energies and entropy corrections were neglected in the present work.

Surface energies of TiO_2 facets were calculated using (1 × 1) slab with thickness of at least six Ti–O layers separated by a vacuum of 15 Å. All the atoms in the slabs were relaxed. Monkhorst–Pack k-points sampling of (6 × 6 × 1) were used for rutile TiO_2(001)-(1 × 1) surface, scaled for other surface energies calculations. The surface energy (γ) is computed using the following expression

$$\gamma = \frac{1}{2A}(E_S - nE_B) \tag{4}$$

where E_s is the total energy of the slab, E_B is the bulk energy per TiO_2 formula, n is the number of TiO_2 formula in the slab, and A is the corresponding surface area of the slab.

3. RESULTS AND DISCUSSION

3.1. Total Activation Energy of Ripening from DFT. The formation energy E_f and the diffusion barrier E_d and the corresponding total activation energy E_{tot} of the Pt monomer on various TiO_2 surfaces in both anatase and rutile phases are given in Table 1. Figure 1a shows the most stable adsorption sites of the Pt monomer on three a-TiO_2 surfaces considered. In the surface layer of a-TiO_2 surfaces considered, Ti_{6c} (six-fold coordinated Ti atom) is not exposed in a(001), but exposed in a(100) and a(101), while Ti_{5c}, O_{2c}, and O_{3c} all are exposed in the three surfaces considered.[44] Due to the absence of the Ti_{6c}, a(001) has more dangling bonds and a higher surface energy γ of 42 meV/Å^2 (in Table S1). As a result, it has the strongest adsorption of the Pt atom and the lowest formation energy E_f of 0.74 eV. Calculated E_f on a(100) is much larger with a value of 2.00 eV, which is still lower than a(101) with a value of 2.46 eV. This can be explained by the difference in the coordination number of the Pt atom with the surface. Figure 1b shows the most stable adsorption sites of the Pt monomer on the four r-TiO_2 surfaces considered. Pt atom coordinates with two

Table 1. Calculated Formation Energy (E_f), Diffusion Barrier (E_d) and Total Activation Energy (E_{tot}) of the Pt Monomer on Various TiO_2 Surfaces in Both Anatase and Rutile Phases

facet	E_f/eV	E_d/eV	E_{tot}/eV
a(001)	0.74	1.02	1.76
a(100)	2.00	0.94	2.94
a(101)	2.46	1.09	3.55
r(001)	0.39	1.33	1.72
r(100)	1.92	1.26	3.18
r(101)	1.45	1.54	2.99
r(110)	3.13	0.43	3.56

DOI: 10.1021/acs.jpcc.9b01942
J. Phys. Chem. C 2019, 123, 11020–11031

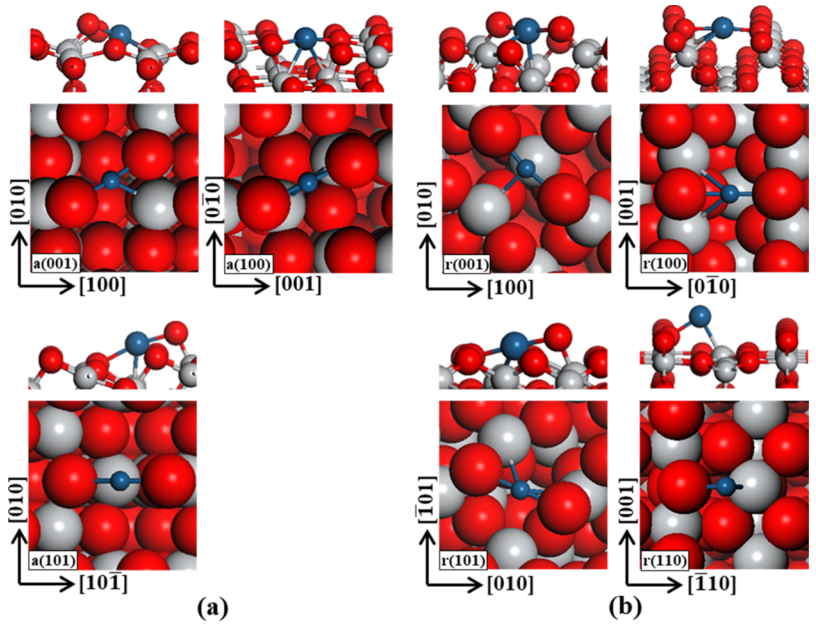

Figure 1. Most stable adsorption sites (side view at the top panel and top view at the bottom panel) of the Pt monomer on anatase TiO_2 a(001), a(100) and a(101) surfaces (a) and rutile TiO_2 r(001), r(100), r(101) and r(110) surfaces (b). Blue, gray and red balls represent Pt, Ti and O atoms respectively.

surface atoms on r(110), but with four atoms on r(001), r(100) and r(101) respectively. We note that the r(110) with the lowest γ of 13 meV/Å^2 (in Table S1) provides the least dangling bonds to stabilize the Pt monomer among all the calculated r-TiO_2 surfaces,[71] and accordingly has the highest E_f of 3.13 eV (Figure 2b). The more unsaturated Ti_{4c} atoms on the r(001) surface with more dangling bonds than that of the Ti_{5c} on the r(100) and r(101) surfaces,[71] are in favor of the formation of the Pt monomer, which rationalizes the lowest E_f of 0.39 eV on r(001). While for r(100) and r(101) surfaces, calculated E_f fall in the middle with value of 1.92 and 1.45 eV, respectively.

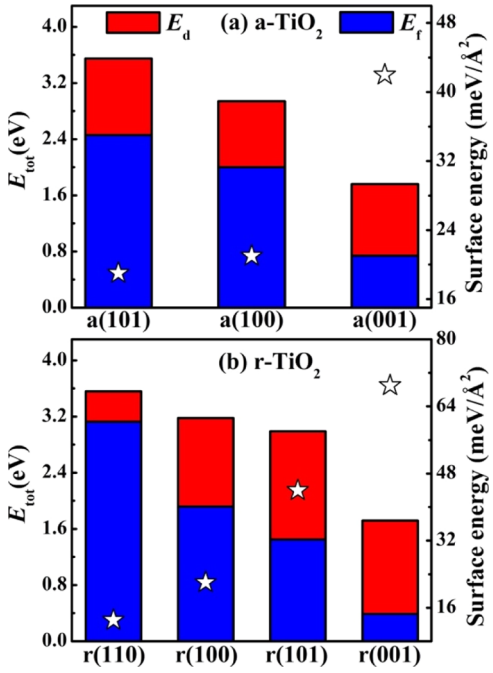

Figure 2. Calculated formation energy E_f (blue), diffusion barrier E_d (red) and total activation energy E_{tot} (=E_f + E_d) of the Pt monomer on anatase TiO_2 surfaces (a) and rutile TiO_2 surfaces (b). Open star is corresponding to the surface energy (meV/Å^2) from our DFT calculations given in Table S1.

For diffusion of the Pt monomer, various diffusion pathways on given surface were considered. The results with a lower barrier are given in Table 1, and the ones with a higher barrier by 0.65 eV in maximum are given in Table S2. The different barriers come mainly from the diffusion along the valley or from one valley to nearest valley, respectively. For the former one, corresponding transition states are shown in Figure S2. It can be found that at most only one Pt−O and one Pt−Ti bond are involved during the diffusion of the Pt monomer on the TiO_2 surfaces considered. This means that the corresponding diffusion barriers would be modest and less sensitive to the surface structures, compared to the formation energies. Indeed, calculated E_d for a-TiO_2 varies only from 0.94 to 1.09 eV, in contrast to E_f varying from 0.74 to 2.46 eV (Figure 2a). For r-TiO_2, though calculated E_d varies considerably from 0.43 to 1.54 eV, the extent of variation remains much smaller than that of E_f varying from 0.39 to 3.13 eV (Figure 2b). It can be found that calculated E_f on r(110), a(100) and a(101) surfaces are at least 1 eV larger than corresponding E_d, a fact that tells that ripening on these surfaces are interface-limit control. Whereas on r(001), calculated E_f are much smaller that of E_d, implying that corresponding ripening process is the diffusion-limit control.

From Figure 2a, it can be found that the calculated total activation energies E_{tot} for a-TiO_2 increases from 1.76 eV for a(001), 2.94 eV for a(100) to 3.55 eV for a(101), respectively. Whereas for r-TiO_2 (Figure 2b), E_{tot} increases from 1.72 eV for r(001), 2.99 eV for r(101), 3.18 eV for r(100) to 3.56 eV for r(110), respectively. These significant numbers indicate that the Pt ripening on both anatase and rutile phases takes place mainly at high temperature. Moreover, calculated E_{tot} varies significantly in magnitude of 1.79 eV for a-TiO_2 and 1.84 eV

DOI: 10.1021/acs.jpcc.9b01942
J. Phys. Chem. C 2019, 123, 11020−11031

for r-TiO_2. This tells that the ripening on both TiO_2 phases are highly sensitive to the crystal surfaces exposed and/or morphologies, as discussed in details below. In Figure 2, the calculated surface energies are also indicated. It can be found that the lower the surface energy, the higher the total activation energy of the ripening monomer, which are understandable. We note that the surfaces with higher surface energies are prone to reconstruct and/or could be stabilized by the reactants,[72] corresponding total activation energy of ripening would change as well. We leave these in future study and restrict here to the pristine and unconstructed surfaces for trend understanding.

3.2. Crystal Surface Dependent Ripening. *3.2.1. Temperature-Programmed Aging.* The temperature programmed aging kinetics of Pt NPs on the r(110) (E_{tot} = 3.56 eV) are studied first and compared with experiments available. The initial PSD with an average size $\langle d_0 \rangle$ = 1.7 nm extracted from the experiment[73] and rsd = 10% are used. The evolution of PSD with a linear temperature ramp from 200 K at a rate of 1 K/s is plotted in Figure 3a. The ripening is found to ignite at approximately 1100 K, along with the decrease in the peak height and right shift in peak position. In line with the evolution of PSD, the average size $\langle d \rangle$ increases from initial 1.7 to 1.8 nm (1100 K), 2.5 nm (1200 K) and 3.9 nm (1300 K) as shown in Figure 3b, respectively. With increase of $\langle d \rangle$, the normalized dispersion and particle number start to decrease accordingly. Compared to the experiment,[73] the calculated growth rate is slightly faster, a fact that might come from the neglection of the influence of oxygen vacancy, underestimating the corresponding total activation energy.[74] For convenience of quantifying the initiation of ripening, we introduce the so-called onset temperature T_{on}, corresponding to about ten percent decrease in the total particle number.[11,37] As indicated in Figure 3b, the calculated T_{on} for the Pt ripening on r(110) is 1074 K.

To see the influence of the TiO_2 surfaces on ripening, the evolution of the average diameter $\langle d \rangle$ of the supported Pt NPs on various TiO_2 surfaces considered with temperature are shown in Figure S3a. It can be found that for Pt NPs on a(001) and r(001), $\langle d \rangle$ starts to increase at low temperature of ~535 K, followed by a(100), r(101) and r(100), whereas on a(101) and r(110), $\langle d \rangle$ starts to increase at high temperature of ~1000 K. For r-TiO_2 (Figure 3c), the calculated T_{on} follows the order of r(001) (535 K) < r(101) (1001 K) < r(100) (1071 K) < r(110) (1208 K), respectively. While for a-TiO_2, it follows the order of a(001) (540 K) < a(100) (980 K) < a(101) (1204 K). Lower T_{on} on a(001) is consistent with experimental observation of the size increase of Pt NPs on a(001) when annealing at 670 K.[75] Significantly higher T_{on} on a(101) and a(100) than a(001) also rationalizes well the better stability for highly dispersed Pt NPs and the absence of sintering on a(101) and a(100), compared to a(001) during CO oxidation.[22] At high temperature, we note that TiO_2 may transit from anatase to rutile, or become mobile and encapsulate the metal NPs, resulting in the so-called strong MSI.[76,77]

The distinct T_{on} tells that different crystal surfaces in both anatase and rutile phases have very different ripening resistance for supported Pt NPs. Irrespective to the anatase and rutile phases considered, a perfect linear correlation between T_{on} and E_{tot} can be seen. Namely, the larger the total activation energy, the higher the onset temperature and the higher the ripening resistance will be, in line with our previous works.[11,37,38,40] Considering the inverse relationship between E_{tot} and γ (Figure 2), this indicates that the surface with a lower surface energy would have a lower ripening tendency for supported metal NPs, not unexpected. On the other hand, the supports with lower γ may interact weakly with the metal NPs, a fact that would make metal NPs mobile, facilitating the PMC process. The overall stability of the supported metal NPs depends therefore on both OR and PMC, which will be reported in our following work.

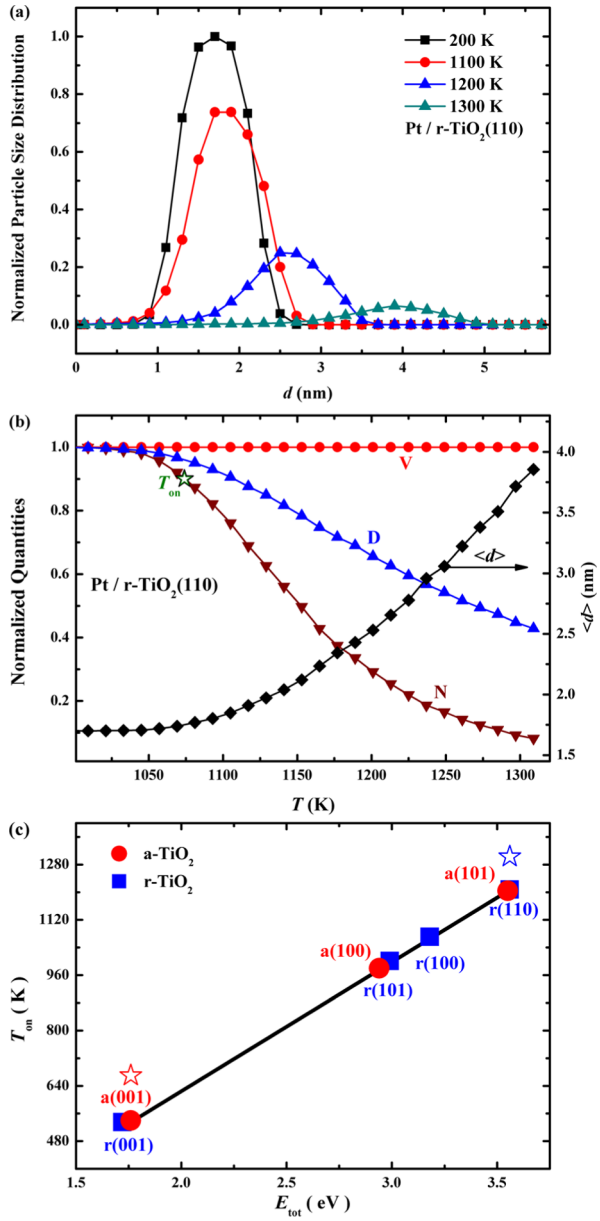

Figure 3. (a) Snapshots of the evolution of particle size distribution for Pt NPs on r-TiO_2(110) and (b) evolution of the normalized volume V (circle), dispersion D (triangle) and particle number N (inverted triangle), and average diameter $\langle d \rangle$ during the temperature ramp; initial $\langle d_0 \rangle$ = 1.7 nm and rsd = 10%, green open star represents onset temperature T_{on}. (c) Calculated T_{on} versus the total activation energies; $\langle d_0 \rangle$ = 3 nm, rsd = 10%, and open stars are value of a(001) (red) and r(110) (blue) from literature.[73,75] γ(Pt) = 155 meV/Å,[59] α = 90°, the temperature ramp starts from 200 K at a rate of 1 K/s.

3.2.2. Isothermal Ripening. The isothermal ripening kinetics of Pt particles on r(110) are performed at 900 K.

DOI: 10.1021/acs.jpcc.9b01942
J. Phys. Chem. C 2019, 123, 11020−11031

The initial PSD with an average size $\langle d_0 \rangle$ = 3 nm and rsd = 10% is used. Snapshots of the resulted PSDs are shown in Figure 4a. (Influence of the PSD on ripening can be found in our recent work for details.[37]) With time progressed, height of the PSD peak decreases gradually along with the right shift in the peak position due to the growth of the larger NPs at the expense of the smaller ones. From Figure 4b, it can be found that the average size increases gradually, and the corresponding (normalized) dispersion and the particle number decrease. While the total volume remains constant since there is no mass loss during the ripening. In Figure 4b, half-life time $t_{1/2}$ for evolution of the particle number[11,37,38,40] is indicated.

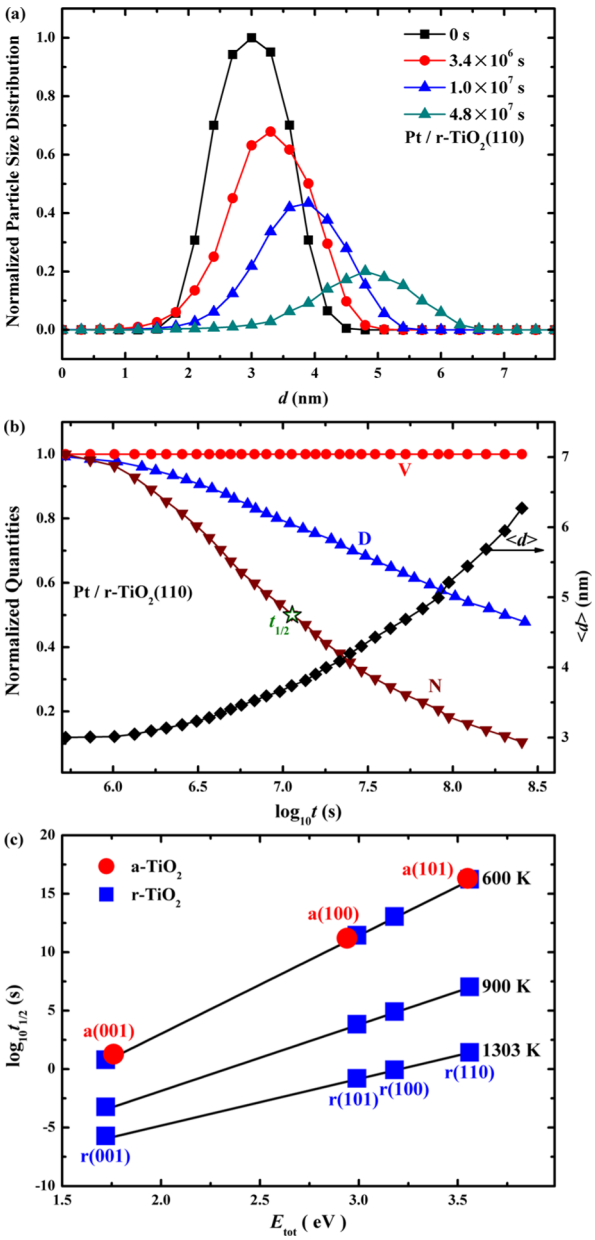

Figure 4. (a) Snapshots of the evolution of partial size distribution and (b) evolution of the normalized volume V (circle), dispersion D (triangle) and particle number N (inverted triangle), and average diameter $\langle d \rangle$ with time for Pt on r(110) at 900 K. Green open star represents half-life time $t_{1/2}$. (c) Calculated half-life time $t_{1/2}$ of Pt on TiO_2 at 600, 900 and 1303 K, respectively. $\langle d_0 \rangle$ = 3 nm, rsd = 10%.

We investigate below the influence of the TiO_2 surfaces on the isothermal ripening. Considering the possible phase transition of a-TiO_2 at elevated temperature, the ripening was simulated first at low temperature of 600 K. Evolution of $\langle d \rangle$ with time (Figure S3b) shows similar trend behavior found under temperature programmed condition. The calculated half-life time $t_{1/2}$ in logarithm with respect to E_{tot} is plotted in Figure 4c. For r-TiO_2, the calculated $t_{1/2}$ follows the same order of r(001) ($\sim 10^1$ s) < r(101) ($\sim 10^{11}$ s) < r(100) ($\sim 10^{13}$ s) < r(110) ($\sim 10^{16}$ s), respectively. While for a-TiO_2, it follows the order of a(001) ($\sim 10^1$ s) < a(100) ($\sim 10^{11}$ s) < a(101) ($\sim 10^{16}$ s). The difference in calculated $t_{1/2}$ between a-TiO_2 (001), (100) and (101) surfaces rationalized well the observed different stability of supported Pt NPs.[22] Note that the calculated $t_{1/2}$ on a(101) and r(110) fall in order of $\sim 10^{16}$ s. This is extraordinary but understandable considering calculated high total activation energies (3.55 and 3.56 eV) and low ripening temperature of 600 K considered. It can be found that the differences of $t_{1/2}$ between the surfaces considered in both anatase and rutile phases are more than ten orders of magnitude, which are huge too. Under realistic condition, the oxide supports might expose different surfaces. The huge difference in $t_{1/2}$ indicates that the ripening process might already be over on specific surfaces with lower total activation energy, but not start yet on other facets with higher total activation energy, which will be explored in details below.

It can be found from Figure 4c that there is again a perfect linear correlation between $t_{1/2}$ (in logarithm) and E_{tot}, as found for T_{on} in Figure 3c. This is interesting since $t_{1/2}$ describes more or less the long-term behavior of ripening under isothermal condition, whereas T_{on} describes mainly the ignition of ripening under temperature-programmed condition. Figure 4c also includes the results at 900 and 1303 K. Since these temperatures are already higher than the phase transition temperature of the anatase TiO_2, only the results of the rutile TiO_2 are plotted. It can be found that with increase of the isothermal temperature from 600 K, to 900 and 1303 K, the linearity remains but corresponding slope gradually decreases. In other words, the difference of the ripening rate between different facets would decrease with temperatures.

3.3. Crystal Morphology Mediated Ripening. Above results show that for the ripening of Pt supported on both anatase and rutile TiO_2, a(001) and r(001) set similar lower limit of T_{on} at ~550 K. While a(101) and r(110) set similar upper limit of T_{on} at ~1200 K. Same can be found for calculated $t_{1/2}$. These imply that the ripening tendency of Pt NPs supported on both crystal phases should be similar, if these surfaces are exposed simultaneously with similar surface ares. To see which surfaces would be exposed and what are their relative ratio occupied, equilibrium morphologies of the pristine bulk are derived and plotted in Figure S4 based on Wulff construction and surface energies calculated by DFT (Table S1). For a-TiO_2, a(101) and a(001) are exposed, occupying about 98 and 2% surface area, respectively. While for r-TiO_2, r(110) and r(101) are exposed, occupying about 85 and 15% surface area. These results are in good agreement with the previous results.[71,78,79] For the pristine a-TiO_2, since the exposed a(001) surface has rather low total activation energy, corresponding oxide as supports works properly at low temperature. Moreover, the potential phase transition from anatase to rutile at approximately 700−900 K[93,94] prevents a-TiO_2 working at high temperature as well. The pristine r-TiO_2 is however very different. Though r(001) also has low total

DOI: 10.1021/acs.jpcc.9b01942
J. Phys. Chem. C 2019, 123, 11020−11031

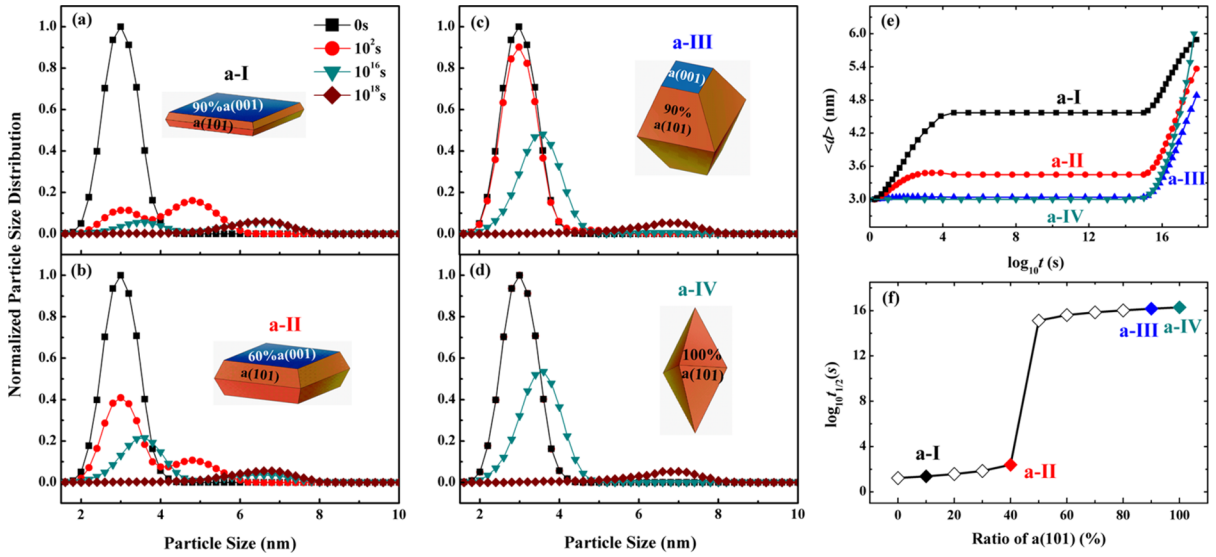

Figure 5. Snapshots of the time evolution of particle size distribution at isothermal temperature of 600 K for Pt on anatase TiO_2 in morphology of (a) **a-I** with 10% of the a(101) facets, (b) **a-II** with 40% of the a(101) facets, (c) **a-III** with 90% of the a(101) facets (d) and **a-IV** with 100% of the a(101) facets at the expense of the a(001) facets. (e) Evolution of the average diameter of Pt NPs on four morphologies with time on stream. (f) Calculated $t_{1/2}$ versus the a(101) ratio. $\langle d_0 \rangle$ = 3 nm, rsd = 10%.

activation energy, according to Wulff construction, it would not be exposed, as found in experiment as well.[80] As a result, r-TiO_2 would be a good support, not only because it is stable at high temperature but also because it is more resistant to the Pt ripening. This rationalizes the experimental observation of the smaller Pt NPs on r-TiO_2 than that on a-TiO_2 after the calcination at 773 K,[30] and the evident growth of Pt on a-TiO_2 NPs at 673 K.[81] This explains the better stability and low ripening tendency found in Ru/TiO_2[33,34] and Co/TiO_2 as well.[35]

3.3.1. Anatase Titanium Oxide. To study explicitly the influence of the oxide morphology on ripening of the supported Pt NPs, we start from the anatase TiO_2. As indicated in Figure S4, corresponding equilibrium morphology from Wulff construction consists of the a(101) and a(001) facets. Compared to ripening on one facets, the ripening processes take places now on two facets with different total activation energies E_{tot} of ripening (3.55 and 1.76 eV) and surface area (98 and 2%). These two factors together lead into a very different kinetics, as seen below. To better explore the influence of the support morphology in term of the relative surface area between two facets, we reform the optimized equilibrium morphology from Wulff construction to four different morphologies noted as **a-I**, **a-II**, **a-III** and **a-IV**, where the ratio of the a(101) facets increases from 10, 40, 90 to 100% at the expense of the a(001) facets (insets in Figure 5a–d), respectively. This is likely thanks to the advance of the shape-controllable synthesis method.[82−87] For simplicity, the corresponding E_{tot} were assumed to be same with the pristine surfaces, and the results with time under the isothermal condition of 600 K are plotted in Figure 5.

For morphology of **a-I** (Figure 5a), it can be found that when the ripening proceeds after a short period of ~10^2 s, there is already a pronounced decrease in the peak height of the PSD. Moreover, the initial monomodal PSD becomes a bimodal PSD. The two peaks have roughly similar height: one is located at initial 3 nm, and another one is located at 4.8 nm. Since the a(001) facets with a lower E_{tot} of 1.76 eV occupy 90% of the surface area exposed, ripening on this facets is fast and results in a new PSD peak at the larger size and a transit bimodal PSD. As seen from Figure 5e, the average diameter (black curve) increases initially with time on stream, but soon becomes constant of ~4.6 nm since ~10^4 s. This is because the ripening on the a(001) facets is already over but it does not start yet on the a(101) facets with a much higher E_{tot} of 3.55 eV. The transit bimodal PSD disappears and becomes monomodal, and there is no change in the (normalized) particle number afterward (Figure S5). Only after a while (at ~10^{15} s), the average diameter starts to increase due to the ignition of the ripening on the a(101) facets. As shown in Figure 5e, this results in a stepwise increase of the average diameter along with the evolution of the PSD with time on stream.

Ripening on morphology of **a-II** is plotted in Figure 5b. Compared to **a-I**, the a(001) ratio decreases from 90 to 60% but remains dominated, while the a(101) ratio increases considerably from 10 to 40%. At t = 10^2 s (Figure 5b), the bimodal PSD appears again. However, the height of the initial PSD peak at 3 nm decreases only modestly, and is much higher than that of the resulted new peak at 4.8 nm. This is because the a(001) ratio is decreased, and its contribution to the overall evolution of the PSD becomes smaller. Increase of the average diameter is paused at ~10^4 s (Figure 5e), similar with **a-I**, since the ripening on the a(001) facets is over. As a result, the bimodal PSD disappears and becomes monomodal. The resulted average value is ~3.4 nm, which is smaller than that of **a-I**, which is understandable. When the ripening on the a(101) facets initiates at ~10^{15} s, the PSD starts to change along with increase of the average size (Figure 5e). With continuous decreasing the a(001) ratio, the height of the second peak in the bimodal PSD decreases gradually. Actually, for morphology of **a-III** with only 10% of the a(001) facets (Figure 5c), the transit bimodal PSD is hardly observed. Meanwhile, there is no stepwise increase in the average diameter with time (Figure 5e). For **a-IV** with 100% of the a(101) facets, the ripening proceeds simply as on domains with same total activation energy (Figure 5d).

DOI: 10.1021/acs.jpcc.9b01942
J. Phys. Chem. C 2019, 123, 11020−11031

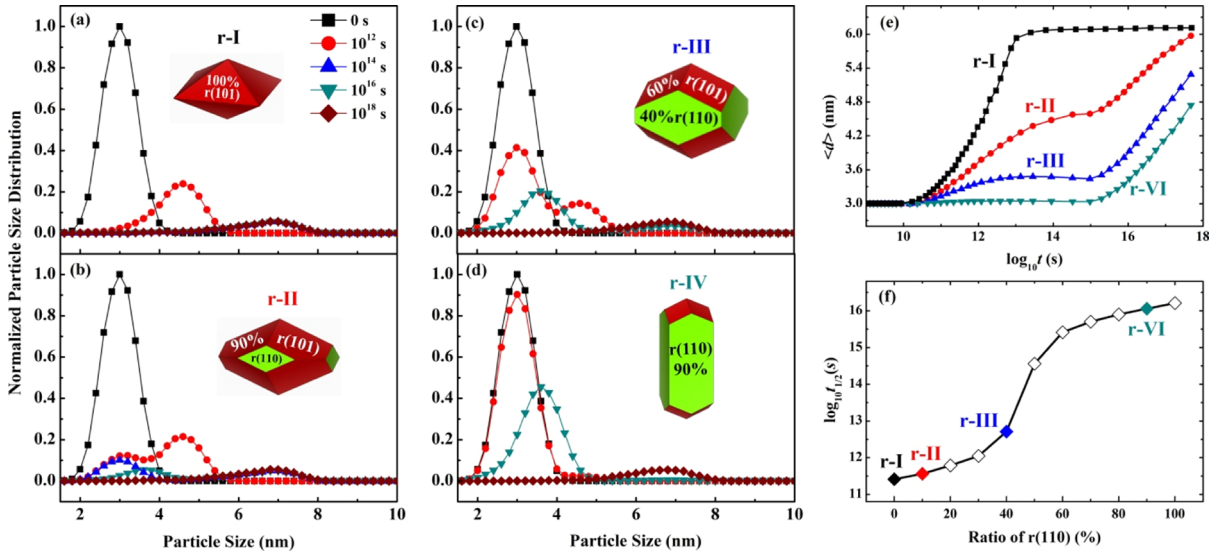

Figure 6. Snapshots of the evolution of particle size distribution at isothermal temperature of 600 K for Pt NPs on r-TiO_2 in morphology of (a) **r-I** with 0% of the r(110) facets, (b) **r-II** with 10% of the r(110) facets, (c) **r-III** with 40% of the r(110) facets (d) and **r-IV** with 90% of the r(110) facets at the expense of the r(101) facets. (e) Evolution of the average diameter of Pt NPs on four morphologies with time on stream. (f) Calculated $t_{1/2}$ versus the r(110) ratio. $\langle d_0 \rangle$ = 3 nm, rsd = 10%.

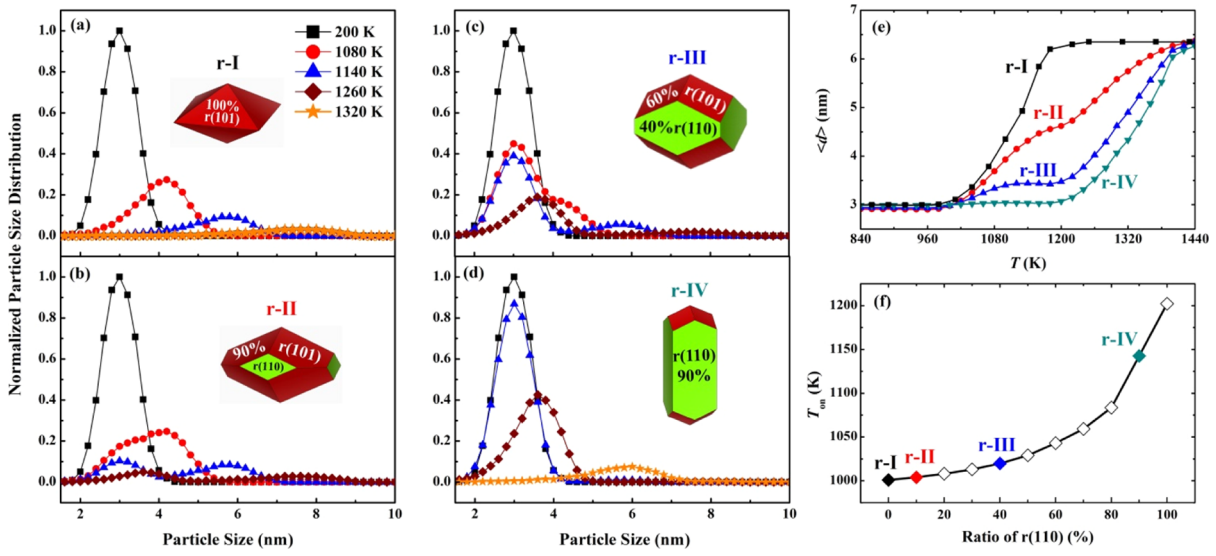

Figure 7. Snapshots of the evolution of particle size distribution for Pt NPs on r-TiO_2 in morphology of (a) **r-I**, (b) **r-II**, (c) **r-III** and (d) **r-IV**, and (e) evolution of the average diameter of Pt NPs on four morphologies of r-TiO_2 with the temperature ramp. (f) Calculated T_{on} with increase of the r(110) ratio. $\langle d_0 \rangle$ = 3 nm, rsd = 10%. The temperature ramp starts from 200 K at a rate of 1 K/s.

The calculated half-life time $t_{1/2}$ with increase of the a(101) ratio at the expense of a(001) is plotted in Figure 5f. Interestingly, the calculated $t_{1/2}$ shows a two-plateau dependence on the a(101) ratio. When the a(101) ratio is less than 40%, corresponding $t_{1/2}$ is located at a low plateau of 10^1 to 10^2 s. This is because the ripening take places first on the a(001) facets, which has higher ripening rate. We note that by definition of $t_{1/2}$, 50% decrease in the total particle number can be therefore realized by ripening on the a(001) facets alone when it occupies more than 50% of surface area. However, when the a(101) ratio is more than 50%, 50% decrease in the total particle number cannot be achieved without initiation of ripening on the a(101) facets. Since the rate of ripening on the a(101) facets is much lower than that of a(001), it leads to a steep jump of $t_{1/2}$ and formation of a higher plateau of 10^{15} to 10^{16} s. It is clear that increasing the amount of the a(001) facets in a-TiO_2 would gradually deteriorate the overall ripening resistance of the supported metal NPs, though the presence of the a(001) facets might promote the catalytic activity as well.[45,88−90] Note that the size-dependent activation energy for ripening monomer attachment due to support surface heterogeneity[91] and surface nucleation inhibited growth[92] for faceted NPs are also proposed to induce the occurrence of transient bimodal distribution.

3.3.2. Rutile Titanium Oxide. We describe here the influence of pristine r-TiO_2 morphology on the ripening of the supported Pt NPs. According to Wulff construction (Figure S4), the pristine r-TiO_2 exposes mainly the r(110) and r(101) facets occupying 85 and 15% of surface area, respectively. In contrast to a-TiO_2, the two facets exposed have closer total activation energies, 3.56 versus 2.99 eV. We note that despite of their close total activation energies, ripening on

DOI: 10.1021/acs.jpcc.9b01942
J. Phys. Chem. C 2019, 123, 11020−11031

the r(110) facets is the interface-limit control, since corresponding formation energy E_f is significantly larger than diffusion barrier E_d (Table 1), whereas on the r(101) facets, both E_f and E_d are similar. To explore the influence of the r-TiO_2 morphology on ripening, we also reform the equilibrium morphology by increase systematically the ratio of the r(110) facets from 0, 10, 40 and 90% at the expense of the r(101) facets, forming four distinct morphology of **r-I**, **r-II**, **r-III** and **r-IV** (see insets in Figure 6a−d), respectively.

The influence of the r-TiO_2 morphology on ripening at isothermal temperature of 600 K can be found in Figure 6. First of all, as found in a-TiO_2 at same isothermal condition, when there are two different facets exposed at the same time, a transit bimodal PSD will be formed (Figure 6b,c). Since both the r(101) and the r(110) facets have a relative larger E_{tot}, the increase in the average diameters becomes considerably only after sufficient long time ($\sim 10^{10}$ s). Accordingly, this postpones dramatically occurrence of the transit bimodal PSD. On the other hand, the difference in E_{tot} of 0.57 eV between two facets is modest, compared to that of 1.79 eV in a-TiO_2. This means that, at the time when ripening on the r(101) facets with a lower E_{tot} is not over yet, ripening on the r(110) facets with a slightly higher E_{tot} could start. In other words, ripening on the r(101) and r(110) facets could contribute to the overall ripening at same time. As a result (Figure 6e), the corresponding average diameter increases monotonically with time, rather than the stepwise increase as found in a-TiO_2. The calculated half-life time versus the r(110) ratio is plotted in Figure 6f. It can be found that $t_{1/2}$ increases monotonically with the r(110) ratio, due to the similar reason indicated above.

Influence of the r-TiO_2 morphology on ripening of the supported Pt NPs under temperature programmed condition is shown in Figure 7. For morphology of **r-I** exposing exclusively the r(101) facets (Figure 7a), the corresponding PSD changes dramatically at temperature of 1080 K. Consistent with the evolution of the PSD, the average diameter for **r-I** increases rapidly after 1080 K but becomes invariable when $T > 1200$ K (Figure 7e). Whereas there is little change in PSD for morphology of **r-IV** dominated by the r(110) facets at 1080 K (Figure 7d), and corresponding average diameter increase pronouncedly only when $T > 1200$ K. Along with increase of the average diameter, the particle number decreases accordingly (Figure S6). When both the r(101) and the r(110) facets are presented in **r-II** (Figure 7b) and **r-III** (Figure 7c), the monomodal PSD changes to a transit bimodal PSD at temperature of 1140 K. In Figure 7f, the onset temperature T_{on} for r-TiO_2 is plotted with respect to the (110) ratio, and monotonic increase of T_{on} from 1000 to 1200 K from **r-I** to **r-IV** shows clearly great impact of the r-TiO_2 morphology on ripening of the supported Pt NPs.

High ripening temperatures found above comes mainly from large total activation energies of the Pt monomer on TiO_2 surfaces considered (Table 1). However, total activation energies of ripening could be reduced in presence of reactants by forming thermodynamically more favorable metal−reactant complexes.[38] As a result, ripening could take places at lower temperatures. Moreover, the reactants could modify the surface properties of supports, a fact of that affects the MSI and total activation energies of ripening as well.[11] All these could influence the corresponding ripening behaviors. The present work focus on the influence of oxide surfaces and crystal phases on ripening of supported metal particles, and their influence on PMC are unclear yet. Since sintering might proceed through either or both PMC and OR, further systematic investigation is necessary. By knowing the structure sensitivity of catalytic reactions, a spatial-resolved evolution of PSD of metal catalysts on oxide supports with various facets exposed are expected to be very helpful for further optimization of the catalytic activity.

4. CONCLUSIONS

In summary, we studied the influence of TiO_2 pristine surfaces and crystal phases on Pt ripening by the first-principles kinetic simulation. For anatase and rutile TiO_2 surfaces considered, it is found that the higher the surface energy of oxide surfaces, the lower the total activation energy will be. Calculated total activation energies on both crystal phases are large and sensitive to the surface orientation, it varies considerably from 1.76 up to 3.56 eV. Pt ripening on TiO_2 would happen typically at elevated temperatures and very sensitive to the oxide morphology. Based on the calculated total activation energies, the intinsic Pt ripening rate of the TiO_2 pristine surfaces follow the order of r(001) ≈ a(001) ≫ a(100) ≈ r(101) > r(100) > a(101) ≈ r(110). For TiO_2 supports exposing different facets, the ripening behavior is determined by not only their intrinsic ripening rate but also their relative surface area, which lead to characteristic transit bimodal PSD. For pristine anatase TiO_2 exposing a(001) and a(101) facets, Pt ripening starts on a(101) facets only after ripening a(001) facets overs, because of their order of magnitude difference in ripening rate, resulting a step-wise increase of the average particle size with ripening time. For pristine rutile TiO_2 exposing r(101) and r(110) facets, Pt ripening initiates first on (101) facets and later on (110) facets. Ripening could proceed simultaneously on both facets due to their modest difference in ripening rate, and corresponding average size increases monotonically. Compared to the pristine rutile TiO_2, the pristine anatase TiO_2 as supports is less resistant to the Pt ripening since a(001) facets with intrinsically high ripening rate is likely to be exposed. Great structural sensitivity of TiO_2 surfaces and crystal phases as supports on ripening of Pt NPs revealed here could be explored in general to more oxides and transition metals, which are valuable to design more stable and efficient catalysts.

■ ASSOCIATED CONTENT

Supporting Information

The Supporting Information is available free of charge on the ACS Publications website at DOI: 10.1021/acs.jpcc.9b01942.

Calculated surface energies (Table S1), transition state positions, evolution of the average diameter of Pt NPs, equilibrium morphologies, and evolution of Pt NP number (Figures S1−S6) can be found in supporting information (PDF)

■ AUTHOR INFORMATION

Corresponding Authors

*E-mail: cqchen@hust.edu.cn (C.C.).
*E-mail: wxli70@ustc.edu.cn (W.-X.L.).

ORCID

Wei-Xue Li: 0000-0002-5043-3088

Author Contributions

⊥Q.W. and S.H. contributed equally.

DOI: 10.1021/acs.jpcc.9b01942
J. Phys. Chem. C 2019, 123, 11020−11031

Notes

The authors declare no competing financial interest.

■ ACKNOWLEDGMENTS

We acknowledge funding from the National Key R&D Program of China (2018YFA0208603, 2017YFB0602205), the Natural Science Foundation of China (91645202), and the Chinese Academy of Sciences (QYZDJ-SSW-SLH054).

■ REFERENCES

(1) Dai, Y.; Lu, P.; Cao, Z.; Campbell, C. T.; Xia, Y. The physical chemistry and materials science behind sinter-resistant catalysts. *Chem. Soc. Rev.* **2018**, *47*, 4314−4331.
(2) Munnik, P.; de Jongh, P. E.; de Jong, K. P. Control and impact of the nanoscale distribution of supported cobalt particles used in Fischer-Tropsch catalysis. *J. Am. Chem. Soc.* **2014**, *136*, 7333−7340.
(3) Saidi, W. A. Density functional theory study of nucleation and growth of Pt nanoparticles on MoS_2(001) surface. *Cryst. Growth Des.* **2015**, *15*, 642−652.
(4) Hansen, T. W.; DeLaRiva, A. T.; Challa, S. R.; Datye, A. K. Sintering of catalytic nanoparticles: particle migration or Ostwald ripening? *Acc. Chem. Res.* **2013**, *46*, 1720−1730.
(5) Pompe, C. E.; Slagter, M.; de Jongh, P. E.; de Jong, K. P. Impact of heterogeneities in silica-supported copper catalysts on their stability for methanol synthesis. *J. Catal.* **2018**, *365*, 1−9.
(6) Song, B.; He, K.; Yuan, Y.; Sharifi-Asl, S.; Cheng, M.; Lu, J.; Saidi, W. A.; Shahbazian-Yassar, R. In situ study of nucleation and growth dynamics of Au nanoparticles on MoS_2 nanoflakes. *Nanoscale* **2018**, *10*, 15809−15818.
(7) Munnik, P.; Velthoen, M. E. Z.; de Jongh, P. E.; de Jong, K. P.; Gommes, C. J. Nanoparticle growth in supported nickel catalysts during methanation reaction-larger is better. *Angew. Chem.* **2014**, *126*, 9647−9651.
(8) Liu, J. J. Advanced Electron Microscopy of Metal-Support Interactions in Supported Metal Catalysts. *ChemCatChem* **2011**, *3*, 934−948.
(9) Goodman, E. D.; Schwalbe, J. A.; Cargnello, M. Mechanistic understanding and the rational design of sinter-resistant heterogeneous catalysts. *ACS Catal.* **2017**, *7*, 7156−7173.
(10) Hu, S.; Li, W.-X. Metal-support interaction controlled migration and coalescence of supported particles. *Sci. China: Technol. Sci.* **2019**, 1−11.
(11) Hu, S.; Li, W.-X. Theoretical investigation of metal-support interactions on ripening kinetics of supported particles. *ChemNanoMat* **2018**, *4*, 510−517.
(12) Lu, P.; Campbell, C. T.; Xia, Y. A sinter-resistant catalytic system fabricated by maneuvering the selectivity of SiO_2 deposition onto the TiO_2 surface versus the Pt nanoparticle surface. *Nano Lett.* **2013**, *13*, 4957−4962.
(13) Li, W.-Z.; Kovarik, L.; Mei, D.; Liu, J.; Wang, Y.; Peden, C. H. F. Stable platinum nanoparticles on specific $MgAl_2O_4$ spinel facets at high temperatures in oxidizing atmospheres. *Nat. Commun.* **2013**, *4*, 2481.
(14) Jones, J.; Xiong, H.; DeLaRiva, A. T.; Peterson, E. J.; Pham, H.; Challa, S. R.; Qi, G.; Oh, S.; Wiebenga, M. H.; Pereira Hernandez, X. I.; et al. Thermally stable single-atom platinum-on-ceria catalysts via atom trapping. *Science* **2016**, *353*, 150−154.
(15) Bruix, A.; Lykhach, Y.; Matolínová, I.; Neitzel, A.; Skála, T.; Tsud, N.; Vorokhta, M.; Stetsovych, V.; Ševčíková, K.; Mysliveček, J.; et al. Maximum noble-metal efficiency in catalytic materials: atomically dispersed surface platinum. *Angew. Chem., Int. Ed.* **2014**, *53*, 10525−10530.
(16) Liu, L.; Ge, C.; Zou, W.; Gu, X.; Gao, F.; Dong, L. Crystal-plane-dependent metal-support interaction in Au/TiO_2. *Phys. Chem. Chem. Phys.* **2015**, *17*, 5133−5140.
(17) Du, X.; Zhang, D.; Shi, L.; Gao, R.; Zhang, J. Morphology dependence of catalytic properties of Ni/CeO_2 nanostructures for carbon dioxide reforming of methane. *J. Phys. Chem. C* **2012**, *116*, 10009−10016.
(18) Liu, J.; Qiao, B.; Song, Y.; Huang, Y.; Liu, J. Hetero-epitaxially anchoring Au nanoparticles onto ZnO nanowires for CO oxidation. *Chem. Commun.* **2015**, *51*, 15332−15335.
(19) Yao, S. Y.; Xu, W. Q.; Johnston-Peck, A. C.; Zhao, F. Z.; Liu, Z. Y.; Luo, S.; Senanayake, S. D.; Martínez-Arias, A.; Liu, W. J.; Rodriguez, J. A. Morphological effects of the nanostructured ceria support on the activity and stability of CuO/CeO_2 catalysts for the water-gas shift reaction. *Phys. Chem. Chem. Phys.* **2014**, *16*, 17183−17195.
(20) Wu, T.; Pan, X.; Zhang, Y.; Miao, Z.; Zhang, B.; Li, J.; Yang, X. Investigation of the redispersion of Pt nanoparticles on polyhedral ceria nanoparticles. *J. Phys. Chem. Lett.* **2014**, *5*, 2479−2483.
(21) Yuan, W.; Zhang, D.; Ou, Y.; Fang, K.; Zhu, B.; Yang, H.; Hansen, T. W.; Wagner, J. B.; Zhang, Z.; Gao, Y.; et al. Direct in situ TEM visualization and insight of the facet-dependent sintering behaviours of gold on TiO_2. *Angew. Chem., Int. Ed.* **2018**, *57*, 16827−16831.
(22) Zhou, Y.; Doronkin, D. E.; Chen, M.; Wei, S.; Grunwaldt, J.-D. Interplay of Pt and crystal facets of TiO_2: CO oxidation activity and operando XAS/DRIFTS studies. *ACS Catal.* **2016**, *6*, 7799−7809.
(23) Wang, R.; Li, Y.; Shi, R.; Yang, M. Effect of metal−support interaction on the catalytic performance of Ni/Al_2O_3 for selective hydrogenation of isoprene. *J. Mol. Catal. A: Chem.* **2011**, *344*, 122−127.
(24) Pang, C. L.; Lindsay, R.; Thornton, G. Structure of clean and adsorbate-covered single-crystal rutile TiO_2 surfaces. *Chem. Rev.* **2013**, *113*, 3887−3948.
(25) Diebold, U. The surface science of titanium dioxide. *Surf. Sci. Rep.* **2003**, *48*, 53−229.
(26) Liu, G.; Yang, H. G.; Pan, J.; Yang, Y. Q.; Lu, G. Q.; Cheng, H.-M. Titanium dioxide crystals with tailored facets. *Chem. Rev.* **2014**, *114*, 9559−9612.
(27) Nguyen, L. Q.; Salim, C.; Hinode, H. Performance of nano-sized Au/TiO_2 for selective catalytic reduction of NO_x by propene. *Appl. Catal., A* **2008**, *347*, 94−99.
(28) Cárdenas-Lizana, F.; Gómez-Quero, S.; Idriss, H.; Keane, M. A. Gold particle size effects in the gas-phase hydrogenation of m-dinitrobenzene over Au/TiO_2. *J. Catal.* **2009**, *268*, 223−234.
(29) Yan, W.; Chen, B.; Mahurin, S. M.; Schwartz, V.; Mullins, D. R.; Lupini, A. R.; Pennycook, S. J.; Dai, S.; Overbury, S. H. Preparation and comparison of supported gold nanocatalysts on anatase, brookite, rutile, and P25 polymorphs of TiO_2 for catalytic oxidation of CO. *J. Phys. Chem. B* **2005**, *109*, 10676−10685.
(30) Iida, H.; Igarashi, A. Characterization of a Pt/TiO (rutile) catalyst for water gas shift reaction at low-temperature. *Appl. Catal., A* **2006**, *298*, 152−160.
(31) Li, Y.; Xu, B.; Fan, Y.; Feng, N.; Qiu, A.; He, J. M. J.; Yang, H.; Chen, Y. The effect of titania polymorph on the strong metal-support interaction of Pd/TiO_2 catalysts and their application in the liquid phase selective hydrogenation of long chain alkadienes. *J. Mol. Catal. A: Chem.* **2004**, *216*, 107−114.
(32) Panpranot, J.; Kontapakdee, K.; Praserthdam, P. Effect of TiO_2 crystalline phase composition on the physicochemical and catalytic properties of Pd/TiO_2 in selective acetylene hydrogenation. *J. Phys. Chem. B* **2006**, *110*, 8019−8024.
(33) Omotoso, T.; Boonyasuwat, S.; Crossley, S. P. Understanding the role of TiO_2 crystal structure on the enhanced activity and stability of Ru/TiO_2 catalysts for the conversion of lignin-derived oxygenates. *Green Chem.* **2014**, *16*, 645−652.
(34) Lin, Q.; Liu, X. Y.; Jiang, Y.; Wang, Y.; Huang, Y.; Zhang, T. Crystal phase effects on the structure and performance of ruthenium nanoparticles for CO_2 hydrogenation. *Catal. Sci. Technol.* **2014**, *4*, 2058−2063.
(35) Xaba, B. M.; de Villiers, J. P. R. Sintering behavior of TiO_2-supported model cobalt Fischer−Tropsch catalysts under H_2 reducing conditions and elevated temperature. *Ind. Eng. Chem. Res.* **2016**, *55*, 9397−9407.

DOI: 10.1021/acs.jpcc.9b01942
J. Phys. Chem. C 2019, 123, 11020−11031

(36) Ouyang, R.; Liu, J.-X.; Li, W.-X. Atomistic theory of Ostwald ripening and disintegration of supported metal particles under reaction conditions. *J. Am. Chem. Soc.* **2013**, *135*, 1760−1771.
(37) Hu, S.; Li, W.-X. Influence of particle size distribution on lifetime and thermal stability of Ostwald ripening of supported particles. *ChemCatChem* **2018**, *10*, 2900−2907.
(38) Hu, S.; Ouyang, R.; Li, W.-X. First-principles kinetics study of carbon monoxide promoted Ostwald ripening of Au particles on FeO/Pt(111). *J. Energy Chem.* **2019**, *30*, 108−113.
(39) Goldsmith, B. R.; Sanderson, E. D.; Ouyang, R.; Li, W.-X. CO- and NO-induced disintegration and redispersion of three-way catalysts rhodium, palladium, and platinum: an ab initio thermodynamics study. *J. Phys. Chem. C* **2014**, *118*, 9588−9597.
(40) Wan, Q.; Hu, S.; Dai, J.; Chen, C.; Li, W.-X. First-principles kinetic study for Ostwald ripening of late transition metals on TiO_2(110). *J. Phys. Chem. C* **2019**, *123*, 1160−1169.
(41) Zhang, B.; Zhang, W.; Su, D. S. Towards a more accurate particle size distribution of supported catalyst by using HAADF-STEM. *ChemCatChem* **2011**, *3*, 965−968.
(42) Fuentes, G. A.; Salinas-Rodríguez, E. Realistic particle size distributions during sintering by Ostwald ripening. *Stud. Surf. Sci. Catal.* **2001**, *139*, 503−510.
(43) Datye, A. K.; Xu, Q.; Kharas, K. C.; McCarty, J. M. Particle size distributions in heterogeneous catalysts: what do they tell us about the sintering mechanism? *Catal. Today* **2006**, *111*, 59−67.
(44) Lazzeri, M.; Vittadini, A.; Selloni, A. Structure and energetics of stoichiometric TiO_2 anatase surfaces. *Phys. Rev. B: Condens. Matter Mater. Phys.* **2001**, *63*, 155409.
(45) Yang, H. G.; Sun, C. H.; Qiao, S. Z.; Zou, J.; Liu, G.; Smith, S. C.; Cheng, H. M.; Lu, G. Q. Anatase TiO_2 single crystals with a large percentage of reactive facets. *Nature* **2008**, *453*, 638−641.
(46) Yang, H. G.; Liu, G.; Qiao, S. Z.; Sun, C. H.; Jin, Y. G.; Smith, S. C.; Zou, J.; Cheng, H. M.; Lu, G. Q. Solvothermal synthesis and photoreactivity of anatase TiO_2 nanosheets with dominant {001} facets. *J. Am. Chem. Soc.* **2009**, *131*, 4078−4083.
(47) Zhu, J.; Wang, S.; Bian, Z.; Xie, S.; Cai, C.; Wang, J.; Yang, H.; Li, H. Solvothermally controllable synthesis of anatase TiO_2 nanocrystals with dominant {001} facets and enhanced photocatalytic activity. *CrystEngComm* **2010**, *12*, 2219.
(48) Yang, X. H.; Li, Z.; Liu, G.; Xing, J.; Sun, C.; Yang, H. G.; Li, C. Ultra-thin anatase TiO_2 nanosheets dominated with {001} facets: thickness-controlled synthesis, growth mechanism and water-splitting properties. *CrystEngComm* **2011**, *13*, 1378−1383.
(49) Amano, F.; Prieto-Mahaney, O.-O.; Terada, Y.; Yasumoto, T.; Shibayama, T.; Ohtani, B. Decahedral single-crystalline particles of anatase titanium(IV) oxide with high photocatalytic activity. *Chem. Mater.* **2009**, *21*, 2601−2603.
(50) Wen, C. Z.; Zhou, J. Z.; Jiang, H. B.; Hu, Q. H.; Qiao, S. Z.; Yang, H. G. Synthesis of micro-sized titanium dioxide nanosheets wholly exposed with high-energy {001} and {100} facets. *Chem. Commun.* **2011**, *47*, 4400−4402.
(51) Parker, S. C.; Campbell, C. T. Kinetic model for sintering of supported metal particles with improved size-dependent energetics and applications to Au on TiO_2(110). *Phys. Rev. B: Condens. Matter Mater. Phys.* **2007**, *75*, 035430.
(52) Johnson, C. A. Generalization of the Gibbs-Thomson equation. *Surf. Sci.* **1965**, *3*, 429−444.
(53) Tran, R.; Xu, Z.; Radhakrishnan, B.; Winston, D.; Sun, W.; Persson, K. A.; Ong, S. P. Surface energies of elemental crystals. *Sci. Data* **2016**, *3*, 160080.
(54) Medasani, B.; Park, Y. H.; Vasiliev, I. Theoretical study of the surface energy, stress, and lattice contraction of silver nanoparticles. *Phys. Rev. B: Condens. Matter Mater. Phys.* **2007**, *75*, 235436.
(55) Farmer, J. A.; Campbell, C. T. Ceria maintains smaller metal catalyst particles by strong metal-support bonding. *Science* **2010**, *329*, 933−936.
(56) Hemmingson, S. L.; Campbell, C. T. Trends in adhesion energies of metal nanoparticles on oxide surfaces: understanding support effects in catalysis and nanotechnology. *ACS Nano* **2017**, *11*, 1196−1203.
(57) Parker, S. C.; Campbell, C. T. Reactivity and sintering kinetics of Au/TiO_2(110) model catalysts: particle size effects. *Top. Catal.* **2007**, *44*, 3−13.
(58) Barnard, A. S.; Zapol, P.; Curtiss, L. A. Anatase and rutile surfaces with adsorbates representative of acidic and basic conditions. *Surf. Sci.* **2005**, *582*, 173−188.
(59) Tyson, W. R.; Miller, W. A. Surface free energies of solid metals: Estimation from liquid surface tension measurements. *Surf. Sci.* **1977**, *62*, 267−276.
(60) Kresse, G.; Furthmüller, J. Efficient iterative schemes for ab initio total-energy calculations using a plane-wave basis set. *Phys. Rev. B: Condens. Matter Mater. Phys.* **1996**, *54*, 11169−11186.
(61) Kresse, G.; Furthmüller, J. Efficiency of ab-initio total energy calculations for metals and semiconductors using a plane-wave basis set. *Comput. Mater. Sci.* **1996**, *6*, 15−50.
(62) Hammer, B.; Hansen, L. B.; Nørskov, J. K. Improved adsorption energetics within density-functional theory using revised Perdew-Burke-Ernzerhof functionals. *Phys. Rev. B: Condens. Matter Mater. Phys.* **1999**, *59*, 7413−7421.
(63) Iddir, H.; Skavysh, V.; Öğüt, S.; Browning, N.; Disko, M. Preferential growth of Pt on rutile TiO_2. *Phys. Rev. B: Condens. Matter Mater. Phys.* **2006**, *73*, No. 041403(R).
(64) Weirich, T. E.; Winterer, M.; Seifried, S.; Mayer, J. Structure of nanocrystalline anatase solved and refined from electron powder data: Presented at the microsymposium onElectron Crystallography of Small Molecules and Organic Materials, 19th European Crystallographic Meeting, Nancy, France, 25-31 August 2000. *Acta Crystallogr., Sect. A: Found. Crystallogr.* **2002**, *58*, 308−315.
(65) Grant, F. A. Properties of rutile (titanium dioxide). *Rev. Mod. Phys.* **1959**, *31*, 646−674.
(66) Feynman, R. P. Forces in molecules. *Phys. Rev.* **1939**, *56*, 340−343.
(67) Kim, H. Y.; Lee, H. M.; Pala, R. G. S.; Shapovalov, V.; Metiu, H. CO oxidation by rutile TiO_2(110) doped with V, W, Cr, Mo, and Mn. *J. Phys. Chem. C* **2008**, *112*, 12398−12408.
(68) Hu, Z.; Metiu, H. Choice of U for DFT+U calculations for titanium oxides. *J. Phys. Chem. C* **2011**, *115*, 5841−5845.
(69) Henkelman, G.; Jónsson, H. Improved tangent estimate in the nudged elastic band method for finding minimum energy paths and saddle points. *J. Chem. Phys.* **2000**, *113*, 9978−9985.
(70) Henkelman, G.; Uberuaga, B. P.; Jónsson, H. A climbing image nudged elastic band method for finding saddle points and minimum energy paths. *J. Chem. Phys.* **2000**, *113*, 9901−9904.
(71) Ramamoorthy, M.; Vanderbilt, D.; King-Smith, R. D. First-principles calculations of the energetics of stoichiometric TiO_2 surfaces. *Phys. Rev. B: Condens. Matter Mater. Phys.* **1994**, *49*, 16721−16727.
(72) Lazzeri, M.; Selloni, A. Stress-driven reconstruction of an oxide surface: the anatase TiO_2(001)-(1×4) surface. *Phys. Rev. Lett.* **2001**, *87*, 266105.
(73) Behafarid, F.; Roldan Cuenya, B. Coarsening phenomena of metal nanoparticles and the influence of the support pre-treatment: Pt/TiO_2(110). *Surf. Sci.* **2012**, *606*, 908−918.
(74) Iddir, H.; Öğüt, S.; Browning, N. D.; Disko, M. M. Adsorption and diffusion of Pt and Au on the stoichiometric and reduced TiO_2 rutile (110) surfaces. *Phys. Rev. B: Condens. Matter Mater. Phys.* **2005**, *72*, No. 081407(R).
(75) Gan, S.; El-azab, A.; Liang, Y. Formation and diffusion of Pt nanoclusters on highly corrugated anatase TiO_2(001)-(1×4) surface. *Surf. Sci.* **2001**, *479*, L369−L374.
(76) Tang, H.; Su, Y.; Zhang, B.; Lee, A. F.; Isaacs, M. A.; Wilson, K.; Li, L.; Ren, Y.; Huang, J.; Haruta, M.; et al. Classical strong metal-support interactions between gold nanoparticles and titanium dioxide. *Sci. Adv.* **2017**, *3*, No. e1700231.
(77) Liu, X.; Liu, M.-H.; Luo, Y.-C.; Mou, C.-Y.; Lin, S. D.; Cheng, H.; Chen, J.-M.; Lee, J.-F.; Lin, T.-S. Strong Metal-Support

DOI: 10.1021/acs.jpcc.9b01942
J. Phys. Chem. C 2019, 123, 11020−11031

Interactions between Gold Nanoparticles and ZnO Nanorods in CO Oxidation. *J. Am. Chem. Soc.* **2012**, *134*, 10251−10258.
(78) Qi, K.; Li, D.; Fu, J.; Zhu, L.; Duan, X.; Qin, Q.; Wang, G.; Zheng, W. Elucidating ionic liquid environments that affect the morphology of TiO_2 nanocrystals: a DFT+D study. *J. Phys. Chem. C* **2014**, *118*, 23320−23327.
(79) Novell-Leruth, G.; Carchini, G.; López, N. On the properties of binary rutile MO_2 compounds, M = Ir, Ru, Sn, and Ti: a DFT study. *J. Chem. Phys.* **2013**, *138*, 194706.
(80) Evarestov, R. A.; Zhukovskii, Y. F. Four-faceted nanowires generated from densely-packed TiO_2 rutile surfaces: Ab initio calculations. *Surf. Sci.* **2013**, *608*, 226−240.
(81) Shiraishi, Y.; Tsukamoto, D.; Sugano, Y.; Shiro, A.; Ichikawa, S.; Tanaka, S.; Hirai, T. Platinum nanoparticles supported on anatase titanium dioxide as highly active catalysts for aerobic oxidation under visible light irradiation. *ACS Catal.* **2012**, *2*, 1984−1992.
(82) Liu, G.; Sun, C.; Yang, H. G.; Smith, S. C.; Wang, L.; Lu, G. Q.; Cheng, H.-M. Nanosized anatase TiO_2 single crystals for enhanced photocatalytic activity. *Chem. Commun.* **2010**, *46*, 755−757.
(83) Amano, F.; Yasumoto, T.; Prieto-Mahaney, O.-O.; Uchida, S.; Shibayama, T.; Ohtani, B. Photocatalytic activity of octahedral single-crystalline mesoparticles of anatase titanium(IV) oxide. *Chem. Commun.* **2009**, 2311−2313.
(84) Menzel, R.; Duerrbeck, A.; Liberti, E.; Yau, H. C.; McComb, D.; Shaffer, M. S. P. Determining the morphology and photocatalytic activity of two-dimensional anatase nanoplatelets using reagent stoichiometry. *Chem. Mater.* **2013**, *25*, 2137−2145.
(85) Fang, W. Q.; Zhou, J. Z.; Liu, J.; Chen, Z. G.; Yang, C.; Sun, C. H.; Qian, G. R.; Zou, J.; Qiao, S. Z.; Yang, H. G. Hierarchical structures of single-crystalline anatase TiO_2 nanosheets dominated by {001} facets. *Chemistry* **2011**, *17*, 1423−1427.
(86) Han, X.; Kuang, Q.; Jin, M.; Xie, Z.; Zheng, L. Synthesis of titania nanosheets with a high Percentage of exposed (001) facets and related photocatalytic properties. *J. Am. Chem. Soc.* **2009**, *131*, 3152−3153.
(87) Ohno, T.; Sarukawa, K.; Matsumura, M. Crystal faces of rutile and anatase TiO_2 particles and their roles in photocatalytic reactions. *New J. Chem.* **2002**, *26*, 1167−1170.
(88) Liu, G.; Pan, J.; Yin, L.; Irvine, J. T. S.; Li, F.; Tan, J.; Wormald, P.; Cheng, H.-M. Heteroatom-modulated switching of photocatalytic hydrogen and oxygen evolution preferences of anatase TiO_2 microspheres. *Adv. Funct. Mater.* **2012**, *22*, 3233−3238.
(89) Tachikawa, T.; Yamashita, S.; Majima, T. Evidence for crystal-face-dependent TiO_2 photocatalysis from single-molecule imaging and kinetic analysis. *J. Am. Chem. Soc.* **2011**, *133*, 7197−7204.
(90) Liu, S.; Yu, J.; Jaroniec, M. Anatase TiO_2 with dominant high-energy {001} facets: synthesis, properties, and applications. *Chem. Mater.* **2011**, *23*, 4085−4093.
(91) Tabib Zadeh Adibi, P.; Zhdanov, V. P.; Langhammer, C.; Grönbeck, H. Transient bimodal particle size distributions during Pt sintering on alumina and silica. *J. Phys. Chem. C* **2015**, *119*, 989−996.
(92) Wynblatt, P.; Gjostein, N. A. Particle growth in model supported metal catalysts-I. Theory. *Acta Metall.* **1976**, *24*, 1165−1174.
(93) Ma, J.-S.; Wen, M.-C.; Lu, C.-H. Reaction mechanism and kinetics analysis of the phase transformation of TiO_2 from the anatase phase to the rutile phase. *J. Mater. Sci.: Mater. Electron.* **2013**, *24*, 2506−2512.
(94) Li, Y.; White, T. J.; Lim, S. H. Low-temperature synthesis and microstructural control of titania nano-particles. *J. Solid State Chem.* **2004**, *177*, 1372−1381.

DOI: 10.1021/acs.jpcc.9b01942
J. Phys. Chem. C 2019, 123, 11020−11031